

INFLUENCES OF INLET SWIRL DISTRIBUTIONS ON AN INTER-TURBINE DUCT PART I: CASING SWIRL VARIATION

Shuzhen Hu¹, Yanfeng Zhang, Xue Feng Zhang

National Research Council Canada
Ottawa, ON, Canada

Edward Vlasic

Pratt & Whitney Canada
Longueuil, QC, Canada

ABSTRACT

The inter-turbine transition duct (ITD) of a gas turbine engine has significant potential for engine weight reduction and/or aerodynamic performance improvement. This potential arises because very little is understood of the flow behavior in the duct in relation to the hub and casing shapes and the flow entering the duct (e.g., swirl angle, turbulence intensity, periodic unsteadiness and blade tip vortices from upstream HP turbine blade rows). In this study, the flow development in an ITD with different inlet swirl distributions was investigated experimentally and numerically. The current paper, which is the first part of a two-part paper, presents the investigations of the influences of the casing swirl variations on the flow physics in the ITD.

The results show a fair agreement between the predicted and experimental data. The radial pressure gradient at the first bend of ITD drives the low momentum hub boundary layer and wake flow radially, which results in a pair of hub counter-rotating vortices. Furthermore, the radially moving low momentum wake flow feeds into the casing region and causes 3D casing boundary layer. At the second bend, the reversed radial pressure gradient together with the 3D casing boundary layer generates a pair of casing counter-rotating vortices. Due to the local adverse pressure gradient, 3D boundary layer separation occurs on both the casing and hub at the second bend and the exit of the ITD, respectively. The casing 3D separation enhances the 3D features of the casing boundary layer as well as the existing casing counter-rotating vortices. With increasing casing swirl angle, the casing 3D boundary layer separation is delayed and the casing counter-rotating vortices are weakened. On the other hand, although the hub swirls are kept constant, the hub counter-rotating vortices get stronger with the

increasing inlet swirl gradient. The total pressure coefficients within the ITD are significantly redistributed by the casing and hub counter-rotating vortices.

INTRODUCTION

The ITD located between the high-pressure turbine (HPT) and low-pressure turbine (LPT) (shown in Figure 1), is a gas turbine component that has been investigated extensively recently. The design of ITDs is likely to become more aggressive with the demands for lighter, more efficient and environment-friendly aircraft engines. Such aggressive inter-turbine transition ducts (AITD) could have shorter axial length and/or larger HPT-to-LPT radial offset, which contains higher risk of boundary layer separation.

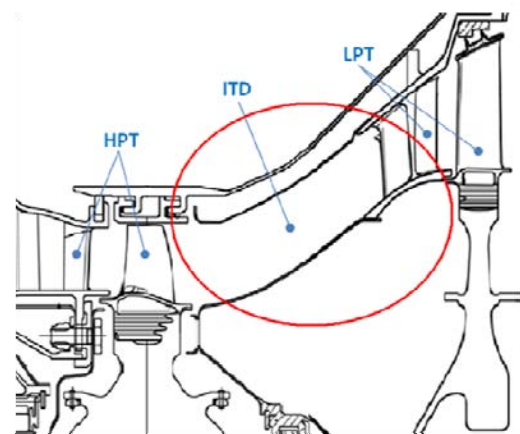


Figure 1. Typical ITD region in a turbofan aeroengine

Hu *et al.* [1] reported that the strong adverse pressure gradient along ITD endwalls caused the boundary layer separation. The endwall static pressure distribution was also significantly influenced by the local curvature distribution. However, if the flow at the entry of an ITD was swirling, the

¹ Ph.D. candidate; Jointly with the Institute of Engineering Thermophysics, Chinese Academy of Sciences.

effective local curvature would be reduced by the longer flow path. Furthermore, to balance the centrifugal force, the local effect of swirling produced a radial pressure gradient, which increased the static pressure along the casing and decreased it along the hub. Therefore, to design the AITD with confidence, the inlet swirl influence on the performance of ITD is necessary to be studied in detail.

The swirl influence in a simple diffuser has been well documented by Bradshaw [2]. The investigations of streamline curvature effects on turbulent flow showed that the swirling flow in an annular passage altered the turbulent structure. This different turbulent structure along the casing and the hub implied the variation in the growth rate of the surface boundary layers and their ability to sustain the adverse pressure gradient. Lohmann *et al.* [3] experimentally studied a series of diffusers with various lengths, area ratios and cant angles under a range of inlet swirl angles. The authors pointed out that the tangential component of the flow was independent of the meridional velocity and the angular momentum was conserved despite the variation in the meridional flow. Kumart *et al.* [4] experimentally investigated the effects of the different inlet swirls through an annular diffuser. It was shown that the increase of inlet swirl reduced the likelihood of casing boundary layer separation. It was therefore suggested that the effect of swirl on the diffuser was possibly greater.

In contrast to the basic diffuser geometries, the inlet swirl effects on the flow in the annular S-shaped diffusers have not been investigated extensively, although, in recently years, many researchers were devoted to the investigation of flow development within an ITD.

Miller *et al.* [5] performed measurements downstream of a single-stage transonic HPT stage to examine the migration and dissipation of flow phenomena (e.g., wakes, vortices, etc.) within an ITD. The results obtained in the absence of the downstream LPT vanes showed that two co-rotating streamwise vortices dominate the flow field. Subsequently, Miller *et al.* [6] carried out the investigation of vane/vortex interaction with a low aspect ratio downstream LPT vanes installed within the ITD. Results showed that the structure of secondary flow in the low aspect ratio vane was changed significantly in the presence of the upstream stage. Marn *et al.* [7] and Göttlich *et al.* [8] investigated the influence of the blade tip gap on the performance of a high-diffusion ITD in a transonic turbine test facility. No separation was detected in the duct. It was observed that CFD could capture the influence of changes in tip clearance on flow field behavior. Additionally, the authors found that the tip clearance flow had a significant effect on the duct performance. Furthermore, Marn *et al.* [9] investigated the effect of tip clearance size on the flow in a super-aggressive ITD which is 20% short than the one in Marn *et al.* [7]. Oil flow visualization results showed full separation along the casing for both gaps. Also the authors pointed out the

vortices at the casing downstream of the first bend are imposed by the upstream HP vanes.

Dominy and Kirkham [10, 11] and Dominy *et al.* [12] were early investigators of the inlet swirl flow influence in an ITD numerically and experimentally. The authors claimed that the swirl modified the static pressure distribution along the endwalls and enhanced the wake skewness. Although the swirl and the wake did not result in large changes in overall loss, the secondary flow structures and the distribution of losses within the duct were affected significantly. Additionally, the predicted results were compared to the experimental data to test the capability of the CFD. It was found that, with no upstream swirl vanes present, the numerical results were in good agreement with the measurements. With swirl vanes located upstream of the ITD, differences between the measurements and computations were observed near the end-walls. Bailey and Carrotte [13] presented a detailed experimental investigation between “clean” and “swirling” case to determine the inlet swirl effects on the flow with an annular S-shape inter-compressor transition duct. The authors found that the tangential momentum was conserved within the duct and the significant change of streamwise pressure gradient was also detected with the effect of inlet swirling flow. Axelsson *et al.* [14], Axelsson and Johansson [15] conducted experimental investigation of flow development within an ITD in a large scale low-speed facility with an HPT stage upstream. An LPT vane ring was installed downstream of the ITD to simulate real exit boundary conditions. Three different operating conditions of the HPT (*i.e.*, varying the rotor speed) were examined. Results showed the absence of end-wall boundary layer separation in the ITD at both the design and off-design conditions. However, at the off-design condition with large swirl angles, a small region of boundary layer separation was detected on the blade suction surface of the LPT vane. The pressure loss coefficient showed that the lowest happened in the design condition and the highest happened in the larger swirl condition. Zhang *et al.* [16] described how the upstream flow field influenced the flow development in the ITD. The radial movement of the low momentum flow driven by the local radial pressure gradient induced a pair of counter-rotating vortices at the hub region. They also claimed that although the numerical simulation had difficulty in capturing the real boundary layer separation, it came close to capturing the flow physics within the ITD.

From the previous work presented above, although the detailed investigation about the inlet swirl influence on the flow development within an ITD had been documented by many researchers, systematic research concerning the effects of inlet swirl has not been conducted yet. The long-term goal of the current project is to parametrically investigate the detailed flow field of modern and aggressive ITDs with upstream HPT stage and downstream LPT vanes as well as the struts inside the ITD. In the current study, the flow development in a modern ITD with different inlet swirl distributions was investigated experimentally and numerically. The different inlet swirl angles

are generated by a swirl vane ring located upstream of the ITD. The present papers focus on improving the physical understanding of the swirl influence on the flow field within the ITD.

Five different inlet swirl distributions were generated by five specifically designed vane rings, which can be classified into two sets. The first set is to keep the hub swirl constant (20°) and to vary the casing swirl (20° , 30° & 40°), while the second set is to keep the casing swirl constant (30°) and to vary the hub swirl (10° , 20° & 30°). The current paper, which is the first part of a two-part paper, presents the experimental and numerical investigations of the casing swirl influence on the flow development of the ITD. The influence of hub swirl variation will be presented in the second part of this paper.

EXPERIMENTAL FACILITY

The investigation was conducted in a large scale, low-speed, axial turbine facility at the National Research Council Canada. A large centrifugal blower draws the air into a settling chamber through a wide-angle diffuser. After the settling chamber, a contraction and an ellipsoidal nose cone guide the flow into an annular section, as shown in Figure 2. To raise the freestream turbulence intensity, a grid made of round-bar mesh can be placed after the contraction, which will produce a freestream turbulence level of 2.3% with an integral length scale of 7 mm at the ITD inlet. A ring of 48 swirl vanes is installed 25 mm upstream of the ITD to provide wakes and swirl to the test section. The ITD test section is an annular test rig with changeable casing and hub sections. The ITD casing can be rotated to provide circumferential traverse for measurements.

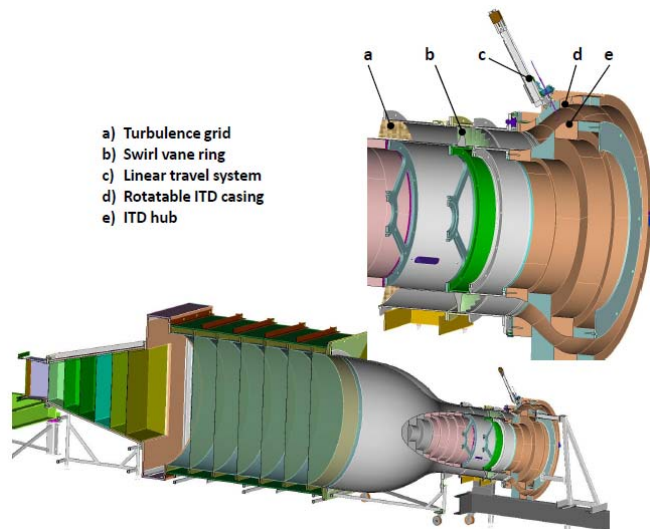


Figure 2. Annular test rig with changeable ITD test section

The current test section, ITD Build A, which is representative of a modern engine design, has a duct outlet-to-inlet area ratio of 1.27 and a mean rise angle of 28° . The

inlet annulus height is 76.2 mm. The non-dimensional duct length (ITD axial length/inlet annulus height) is 3.4.

In the present experiment, an L-shaped seven-hole pressure probe with a tip diameter of 1.6 mm and a tip cone included angle of 30° was used for detailed 2D mapping measurement. The measurement grid in each plane consists of at least 31 points radially and 31 points circumferentially to cover one upstream swirl vane passage (7.5°). The first measurement point was placed as close as 0.5 mm to both hub and casing surfaces with the distance between positions increasing exponentially as the probe was retracted from the surfaces. One row of 40 static pressure taps is distributed along the ITD rotatable casing. Two rows of 40 static pressure taps with half pitch spacing are distributed along the stationary ITD hub. Surface oil flow visualization was also used to examine the flow behavior on both hub and casing surfaces. A mixture of alkali refined linseed oil and titanium dioxide powder was applied in an extremely thin layer over the surfaces. After letting the tunnels run at condition for roughly 30 minutes, the parts were removed and photographed.

The measurement locations in the ITD test section are shown in Figure 3. Location R is 300 mm upstream of the swirl vane ring and is used to provide tunnel operation reference as well as the boundary conditions for the numerical simulation. A linear traverse system can be mounted on the rotatable ITD casing to provide full area traversing at five different planes (A1 to A5). Location A1 is at the ITD inlet plane and Location A5 is at the ITD outlet plane. Three more traverse planes (A2, A3 and A4) were placed inside the duct and roughly perpendicular to both hub and casing surfaces. Figure 3 also gives the coordinate system, which was based on the local measurement plane.

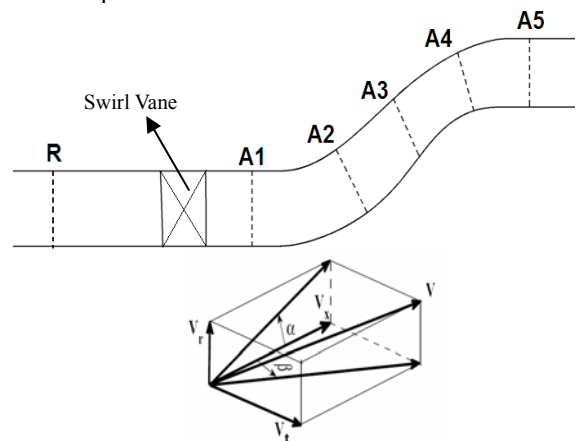


Figure 3. Measurement locations and coordinate system

The wind tunnel operating conditions were monitored using static pressure taps located at the inlet of the contraction and the reference Location R. A tunnel operating coefficient was used to obtain the freestream velocity at Location R. All the pressure values are measured by using a Scanivalve DSA 3217 pressure scanner. The scanner has sixteen temperature compensated differential pressure transducers with a

measurement range of ± 1250 Pa. The uncertainty in the measured pressure is estimated to be better than 0.05% of the transducer's full-scale range. The uncertainties in the measured dynamic and total pressures are estimated to be $\pm 0.5\%$ and $\pm 0.25\%$ respectively of the reference dynamic pressure. The Reynolds number, based on the height of the ITD inlet and the freestream velocity at location R , is 150,000 in all test cases.

NUMERICAL METHOD

The numerical simulation was performed using NUMECA Fine/Turbo 8.7.3. The steady-state flow solution was achieved with the convergence of a 4-stage explicit Runge-Kutta integration scheme. The time-marching algorithm was stabilized using scalar eigenvalue-based second- and fourth-order difference smoothing operators. In order to speed up the convergence to a steady state, local time stepping, residual smoothing and multigrid techniques were applied. The turbulent closure was achieved with *SST* (Shear Stress Transport) turbulence model after a comparison of different turbulence models by Zhang *et al.* [16].

The inlet boundary condition for the simulations was established with measured velocity profiles, turbulence intensity profiles and turbulent length scale profiles at location R . The outlet boundary condition was set as uniform atmospheric pressure. No slip and heat transfer conditions were imposed at all solid boundaries. The grid topology consisted of approximately 3.17 million nodes, determined from a grid independence study, and y^+ was equal to or smaller than 2.

INLET FLOW CONDITION

The designed swirl distributions of the three vane rings presented in this paper are summarized in Table 1. The three swirl vane rings, namely test cases A, B and C, have the same hub swirl angle of 20° , while the casing swirl angles are 20° , 30° and 40° , respectively. The swirl gradients ($\beta_{\text{casing}} - \beta_{\text{hub}}$) of cases A, B and C are 0° , 10° and 20° , respectively. The mean swirls of cases A, B and C are 20° , 25° and 30° , respectively.

Test Case	Hub Swirl	Casing Swirl	Mean Swirl	Swirl Gradient
A	20°	20°	20°	0°
B	20°	30°	25°	10°
C	20°	40°	30°	20°

Table 1. Summary of swirl distributions for the three vanes

Figure 4 shows the experimental and numerical radial distributions of the pitchwise mass-averaged swirl angles, β , and the total pressure coefficients, Cp_0 , at Location A1. From Figure 4, the numerical results match with experimental results reasonably well. And the deliberately

designed casing swirl variation from 20° to 40° for the three cases is clearly seen in Figure 4(a) both in CFD and experimental data. The experimental and numerical total pressure coefficient distributions at the inlet of ITD with different casing swirl angles are almost identical as shown in Figure 4(b). This suggests the inter-turbine duct is being tested under the similar inlet conditions but with different casing swirl angles.

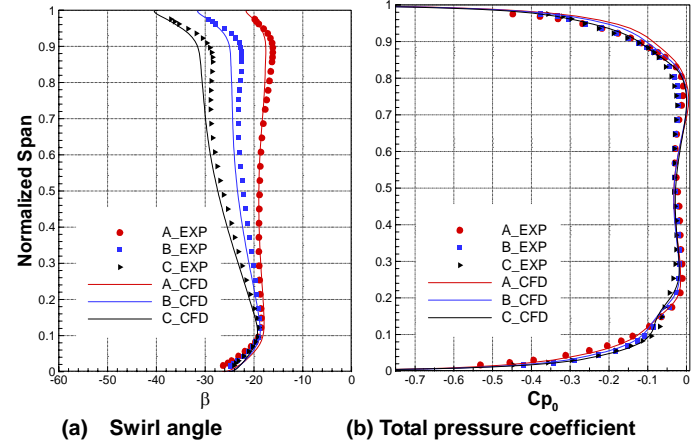


Figure 4. Pitchwise mass-averaged swirl angle β and total pressure coefficient Cp_0 at Location A1

RESULTS AND DISCUSSION

The predicted pitchwise mass-averaged static pressure coefficients, Cp_s , in test case A (top) and the experimental area-

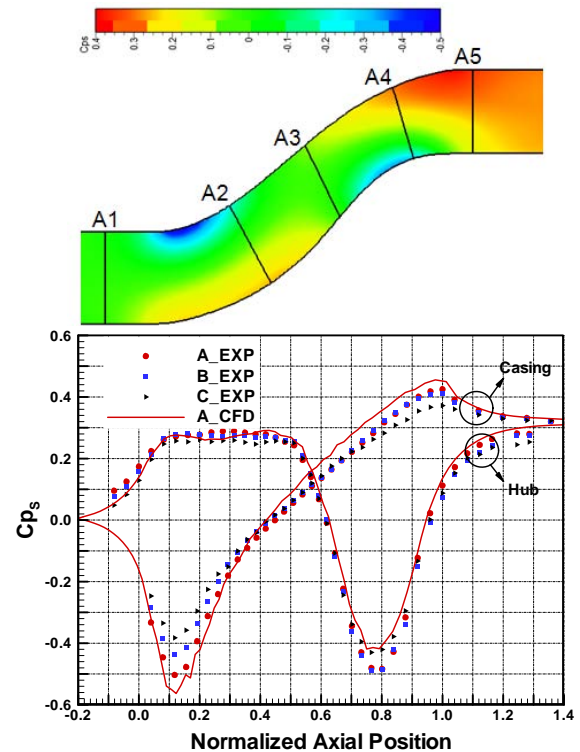


Figure 5. Static pressure coefficients inside the ITD (top) and along the hub and casing (bottom)

averaged static pressure coefficients along the ITD endwalls in the three test cases (bottom), are presented in Figure 5. The axial positions 0 and 1 in Figure 5 are represented the first and last points of curvature change of the endwalls, respectively. The axial positions of Location A1 to A5 correspond to the positions on the contoured plot.

As shown in Figure 5, along the casing, there is a favorable pressure gradient before the first bend, followed by a strong adverse pressure gradient between the first and second bends and then a weak favorable pressure gradient until the exit. The strong adverse pressure gradient over a large portion of the casing causes the boundary layer to separate, which will be shown in the flow visualization. Along the hub, there is an adverse pressure gradient before the first bend, and then the static pressure stays almost constant until the second bend. There, a favorable pressure gradient is followed by a strong adverse pressure gradient from the second bend to the exit. The adverse pressure gradient in the two regions may cause boundary layer separation at the hub as well. Furthermore, due to the increasing effective flow area and the endwall curvature, at the first bend, the static pressure at the casing is lower than

that at the hub, while the opposite is true at the second bend. These radial pressure gradients tend to move fluid radially. Additionally, the numerical static pressure distribution captures the flow trend reasonably well. The difference between numerical and experimental data is mainly in the second bend where the flow phenomenon is more complicate.

Flow Development in ITD

The comparison in Figure 4 and Figure 5 shows that CFD results can capture the flow trend reasonable well. To further validate the CFD results, the numerical and experimental flow development in test case A are compared and the detailed flow physics are discussed in this section. The predicted and experimental total pressure coefficient isolines superimposed on the streamwise vorticity coefficient contours within the ITD from Location A1 to A5 are presented in Figure 6. The results above the hub are the CFD results (CFD) while those underneath the hub are the corresponding experimental results (EXP). The casing wall shear stress vectors are plotted as green lines in the figure as well.

The streamwise vorticity coefficient, C_{os} , is the normalized streamwise vorticity. For both experimental and numerical data, the streamwise vorticity is defined as:

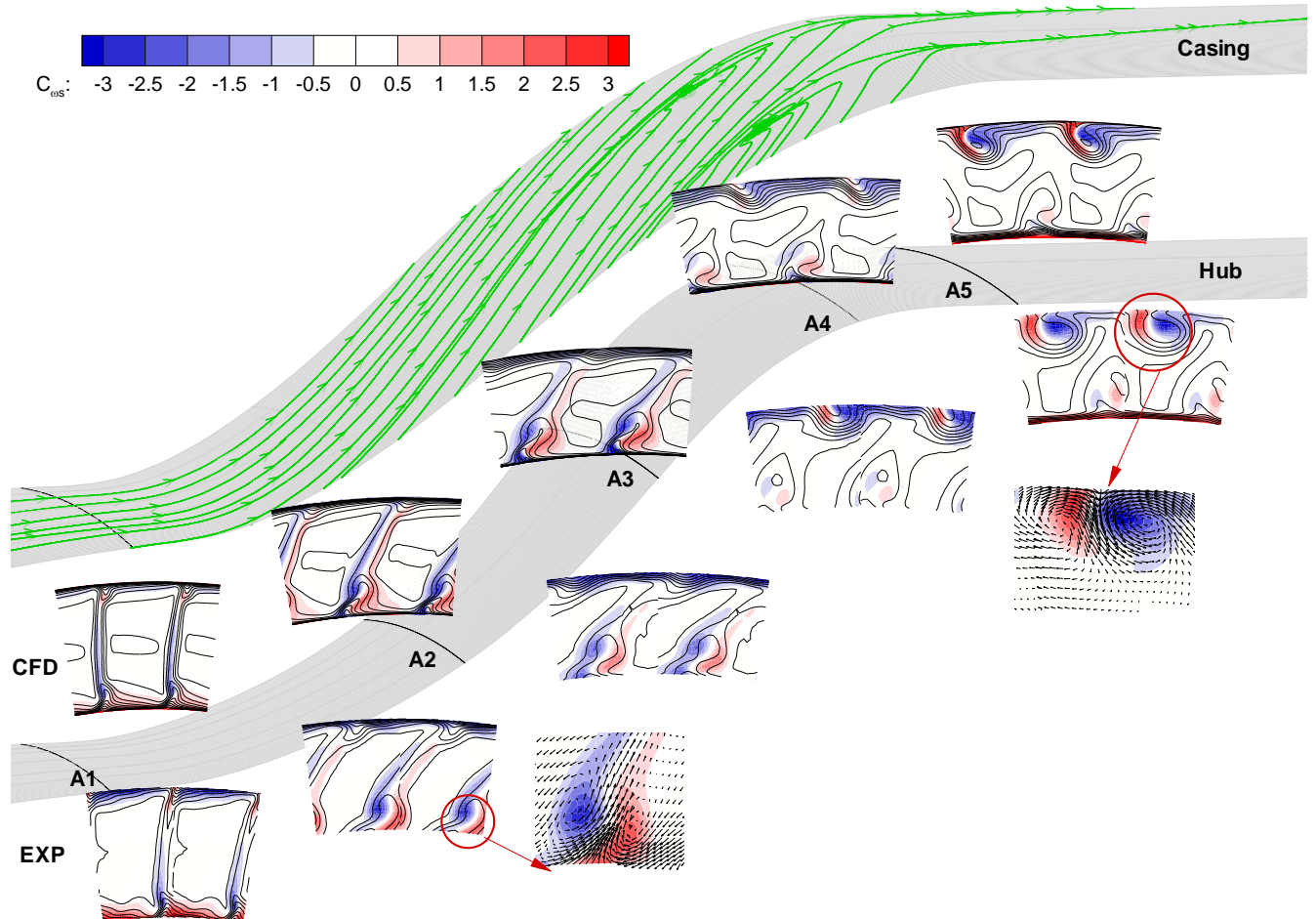


Figure 6. Total pressure coefficient isolines and streamwise vorticity coefficient contours for test case A (20°, 20°)

$$\omega_s = \frac{\omega_x V_x + \omega_t V_t + \omega_r V_r}{\sqrt{V_x^2 + V_t^2 + V_r^2}}$$

The components of the predicted vorticity vector in cylindrical coordinates are calculated as:

$$\omega_x = \frac{1}{r} \left(\frac{\partial(rV_t)}{\partial r} - \frac{\partial V_r}{\partial t} \right)$$

$$\omega_t = \left(\frac{\partial V_r}{\partial x} - \frac{\partial V_x}{\partial r} \right)$$

$$\omega_r = \left(\frac{1}{r} \frac{\partial V_x}{\partial t} - \frac{\partial V_t}{\partial x} \right)$$

To calculate the streamwise vorticity from the measurement, estimations of velocity gradients in both radial and circumferential directions can be obtained easily. However, it is much more difficult to estimate the axial velocity gradients due to the large axial space between measuring planes. Thus, only ω_x can be obtained from the measurements directly. However, following the method of Yaras and Sjolander [17], assuming steady incompressible flow, neglecting the viscous term, the other two components can also be obtained from the measurements as follow.

$$\omega_t = \frac{1}{V_x} \left(V_t \omega_x - \frac{1}{\rho} \frac{\partial p_0}{\partial r} \right)$$

$$\omega_r = \frac{1}{V_x} \left(V_r \omega_x + \frac{1}{\rho r} \frac{\partial p_0}{\partial t} \right)$$

In this paper, all the vorticity components are normalized by $U_{ref}/\Delta R$, where U_{ref} is the reference velocity at location R and ΔR is the annulus height ($R_{casing}-R_{hub}$) at the ITD inlet.

As shown in Figure 6, the predicted results successfully capture the hub and casing boundary layer developments and the streamwise vorticity structures, which are the key fluid mechanisms within the ITD. The main difference between these two results is only the magnitude. In this section, the general flow development will be investigated by both experimental and computational results and the detailed flow physics within the ITD will be discussed using the simulation results.

In the hub region, at the ITD inlet (Location A1), streamwise vorticity structures are dominated by the negative wake vorticity and the positive passage vorticity, as shown in Figure 6. These vorticity regions grow up as flow convecting from Location A1 to A2. Due to the radial movement of the low momentum hub boundary layer and wake flow caused by the local radial pressure gradient, a pair of hub counter-rotating vortices is formed. These hub counter-rotating vortices locate at about 25% of the channel height and accumulate the hub region low momentum flow to form a high loss core at Location A2. Due to the radial movement of the hub boundary layer and the favorable pressure gradient along the hub, the hub boundary layer remains relatively thin at Locations A2, A3 and A4. The hub boundary layer separates around Location A5 with highly

3D features due to the streamwise adverse pressure gradient close to the exit. A more detailed discussion about the flow development in the hub region is presented in Part II of this study.

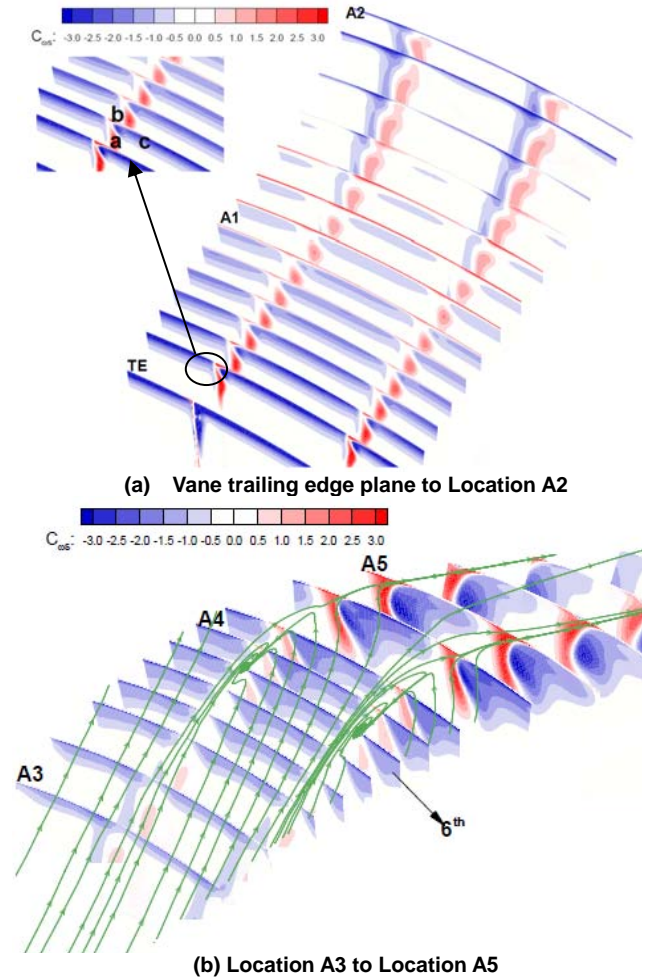


Figure 7. Predicted casing streamwise vorticity coefficient C_{ω_s} from Trailing edge to Location A5 for case A (20° , 20°)

Figure 7 presents the detail flood contours of the predicted casing streamwise vorticity at different axial planes within the ITD between the swirl vane trailing edge and Location A5 for case A. From Figure 7(a), in the casing region, downstream of the swirl vanes, the casing streamwise vorticities are dominated by the trailing shed vorticity (a), corner vorticity (b) and passage vorticity(c). These vortices are dissipated as they travel downstream and are almost mixed out at Location A2. In the casing region, the upstream vane casing vorticity field has slight influence on the ITD casing region flow field. However, at the first bend, the radial pressure gradient drives the low momentum flow radially feeding into the casing boundary layer region. Together with the strong casing streamwise adverse pressure gradient after Location A2, the low momentum flow accumulates into a low momentum core and causes the casing boundary layer with strong 3D features, which can be detected at Location A3. As shown in Figure 5, at the first bend, the

radial pressure gradient in the casing region is relatively weak; therefore, the casing counter-rotating vortices are difficult to generate. Downstream of Location A3, the radial pressure gradient is reversed as shown in Figure 5. Due to the pronounced casing 3D boundary layer and the reversed radial pressure gradient, a pair of casing counter-rotating vortices is generated at Location A4. Additionally, from Location A3 to Location A4, due to the strong local adverse pressure gradient, casing 3D boundary layer separation occurs in this region as shown in Figure 5 and 7(b).

From Figure 7(b), at the 6th slice downstream of Location A3, a pair of casing counter-rotating vortices is generated due to the radial movement of the low momentum core in the 3D casing boundary layer driven by the reversed casing radial pressure gradient. Additionally, slightly downstream of the 6th slice, the casing 3D boundary layer separation first occurs in the casing counter-rotating vortices region, essentially in the low momentum core region. This is because the low momentum core is more easily separated under the strong adverse pressure gradient. Furthermore, the casing counter-rotating vortices have significant influence on this casing boundary layer 3D separation. The flow in the positive vorticity region produces a tangential velocity with a direction opposite to the mean flow swirl direction, which causes a stronger streamwise adverse pressure gradient. Hence, the boundary layer separation in the positive vorticity region is stronger. The casing 3D separation enhances the 3D casing boundary layer development as well as the casing counter-rotating vortices. At Location A5, the casing counter-rotating vortices are further enhanced by the second bend radial pressure gradient and the casing 3D boundary layer separation. Downstream of Location A5, these casing counter-rotating vortices start to dissipate.

To clarify the origin of the two pairs of streamwise vorticity, the experimental secondary velocity vectors, which represent the deviation of the local velocity from the pitchwise mass-averaged velocity, are superimposed on the streamwise vorticity contours at Locations A2 and A5 in Figure 6. The secondary flow vectors show that the directions of the casing counter-rotating vortices are opposite to the hub counter-rotating vortices. This confirms that the hub counter-rotating vortices are generated by the radial pressure gradient at the first bend, which drives the low momentum flow from the hub to casing; while the casing counter-rotating vortices are generated by the reversed radial pressure gradient at the second bend, which is from the casing to the hub.

Another phenomenon within the ITD deserving comment is the wake tilt. As documented by Brookfield *et al.* [18], the main sources of wake tilt are the initial blade twist angle, and the axial and tangential velocities. Due to the conservation of angular momentum, the tangential velocity decreases with the radius increase within the ITD. The local axial velocity is changed based on the increasing

effective flow area and wall curvature. The axial velocity along the ITD hub decreases at the first bend, increases between the first and second bends, and then decreases again until the exit. The opposite occurs at the ITD casing region. Therefore, at the first bend, the casing region swirl angle is reduced more quickly than the hub swirl, resulting in clockwise wake tilt. At the second bend, the hub swirl angle is decreased more rapidly than the casing swirl, which leads to a counter-clockwise wake tilt. Therefore, the wake is tilted clockwise at the first bend and counter-clockwise at the second bend. For easy discussion, the wake skew angle is used in this paper, which is defined as the angle between the wake centre line and the vertical plane. As shown in Figure 6, the wake skew angle is 30° in clockwise direction at the first bend, and then is gradually decreased at the second bend. The wake skew angle will influence the casing 3D boundary layer development, which will be discussed in more detail later.

Based on the discussion above, the flow development within ITD is dominated by the hub and casing counter-rotating vortices as well as the hub and casing 3D boundary layer separations. The following section will focus on the discussion of the influences of the casing swirl angle variations on the flow development within the ITD. All the results presented in the following are achieved through detailed measurements.

Influences of Casing Swirl Variation

The ITD wall static pressure distributions presented in Figure 5 show that the casing streamwise adverse pressure gradient between the first and second bends is reduced as the casing swirl is increased from 20° to 40°. The higher casing swirl angle results in a longer flow path through the duct, and therefore reduces the effective flow curvature and decreases the streamwise pressure gradient correspondingly. Although the hub swirls are constant in the three test cases, the hub streamwise pressure gradient is changed with different casing swirl angles, especially for the case C with 40° casing swirl at the second bend of the ITD. Furthermore, due to the change of the casing and hub static pressure distributions, the radial pressure gradient is changed correspondingly. As shown in Figure 5, the higher radial pressure gradients can be detected at both the first and second bends of the ITD with the lower inlet casing swirl angle.

In order to investigate the influences of different swirl angles on casing endwall flow behaviors, Figure 8 presents the casing flow visualization for the three test cases. The measurement locations, A2 to A5, are also labeled in the flow visualization photos for easy analysis.

As shown in Figure 8(a), the test case A (20°, 20°), the high shear stress region, which is caused by the upstream wakes and marked as *L1*, shows that the flow angle gradually increases due to the effect of the curvature and the angle momentum conservation. Downstream of Location A3, the casing boundary layer separation occurs, marked as *S1* in the figure. This casing boundary layer separation contains very strong 3D features and persists until Location A4. The weak casing

counter-rotating vortices upstream the 3D casing boundary layer separation are hard to be detected in the flow visualization. Downstream of the separation region, between Locations A4 and A5, a pair of pronounced counter-rotating streamwise vortices is detected in the flow visualization as a narrow low shear stress region with two high shear stress strips at each side.

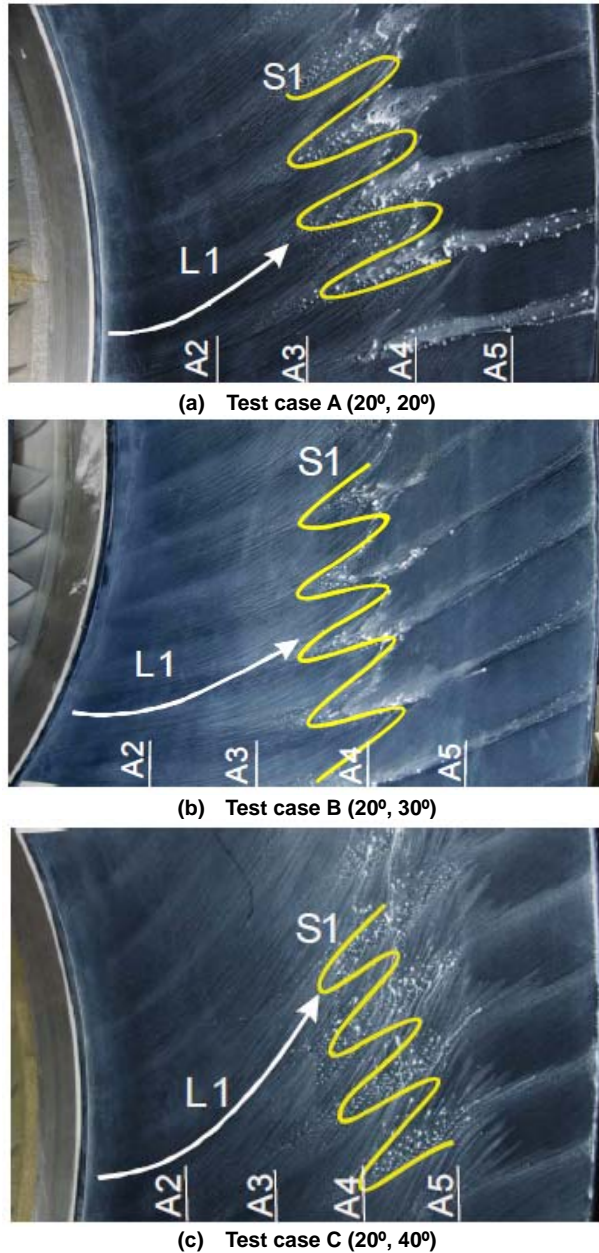


Figure 8. Casing flow visualization for three test cases

In Figure 8(b), the test case B (20°, 30°), the wake flow labeled as *L1* has a larger swirl and a longer flow path. The onset of the casing 3D boundary layer separation is delayed and it is weaker than that in case A. This is due to the weaker casing streamwise adverse pressure gradient as shown in Figure 5. The casing counter-rotating vortices are

detected after the casing 3D separation region and persist until the exit of the ITD as well.

In Figure 8(c), the test case C (20°, 40°), the wake flow *L1* shows a longer flow path compared with those both in case A and B. However, it is noted that, downstream Location A3, it is difficult to distinguish the wake flow. This infers that the wake flow near the casing is almost mixed out at this location and casing boundary layer contains less 3D feature. The casing 3D boundary layer separation occurs very close to Location A4. Compared with the results in both cases A and B, the separation is further delayed and much weaker. This is also because the presence of the lowest streamwise adverse pressure gradient in this test case as shown in Figure 5. At Location A5, the casing counter-rotating vortices are found in flow visualization. A detailed comparison of the flow development in the three test cases will be presented next.

The contours of the total pressure coefficients, C_{p0} , and the streamwise vorticity coefficients, C_{os} , at different streamwise locations (A1 to A5) for the three test cases are presented in Figure 9. The isolines of C_{p0} are superimposed on the contour plots as well.

At the ITD inlet (Location A1), the upstream wakes and swirl distributions can be clearly detected by the deficit of the total pressure. The casing swirl angles change from 20° to 40°, shown in Figure 9(a), 9(b) and 9(c), respectively. The magnitudes of the total pressure coefficients at Location A1 are almost the same, which is desirable. The primary difference among the three cases is the magnitude of the wake vorticity. The wake flow with the highest swirl gradient in test case C contains the strongest wake vorticity. The swirl gradient causes the wake flow stretching, which leads to an increase in the strength of the wake vorticity. The increase of wake vorticities due to the wake stretching was also documented by Brookfield *et al.* [18].

At Location A2, the casing counter-rotating vortices have been not formed yet in any of the three cases. The casing boundary layer appears to have 3D features with a low momentum core although it is not pronounced. In cases A and B, the wake skew angle is 30° and 0° in the clockwise direction respectively. In case C, the wake skew angle is 20° in counter-clockwise direction. The wake skew angle is influenced by the combined effects of the inlet swirl gradient, the first bend clockwise tilt and the second bend counter-clockwise tilt as discussed before. The hub counter-rotating vortices are detected in all three test cases and with well-formed loss cores. Comparing the hub counter-rotating vortices in the three cases, the weakest occurs in case A and the strongest occurs in case C. As discussed in Part II of this study (Zhang *et al.* [19]), the upstream wake vorticity also has significant influence on the hub counter-rotating vortices. The weakest upstream wake vorticity in test case A induces the weakest hub counter-rotating vortices and the strongest upstream wake vorticity in test case C induces the strongest hub counter-rotating vortices. Additionally, the hub boundary layer at Location A2 remains very thin in all three cases.

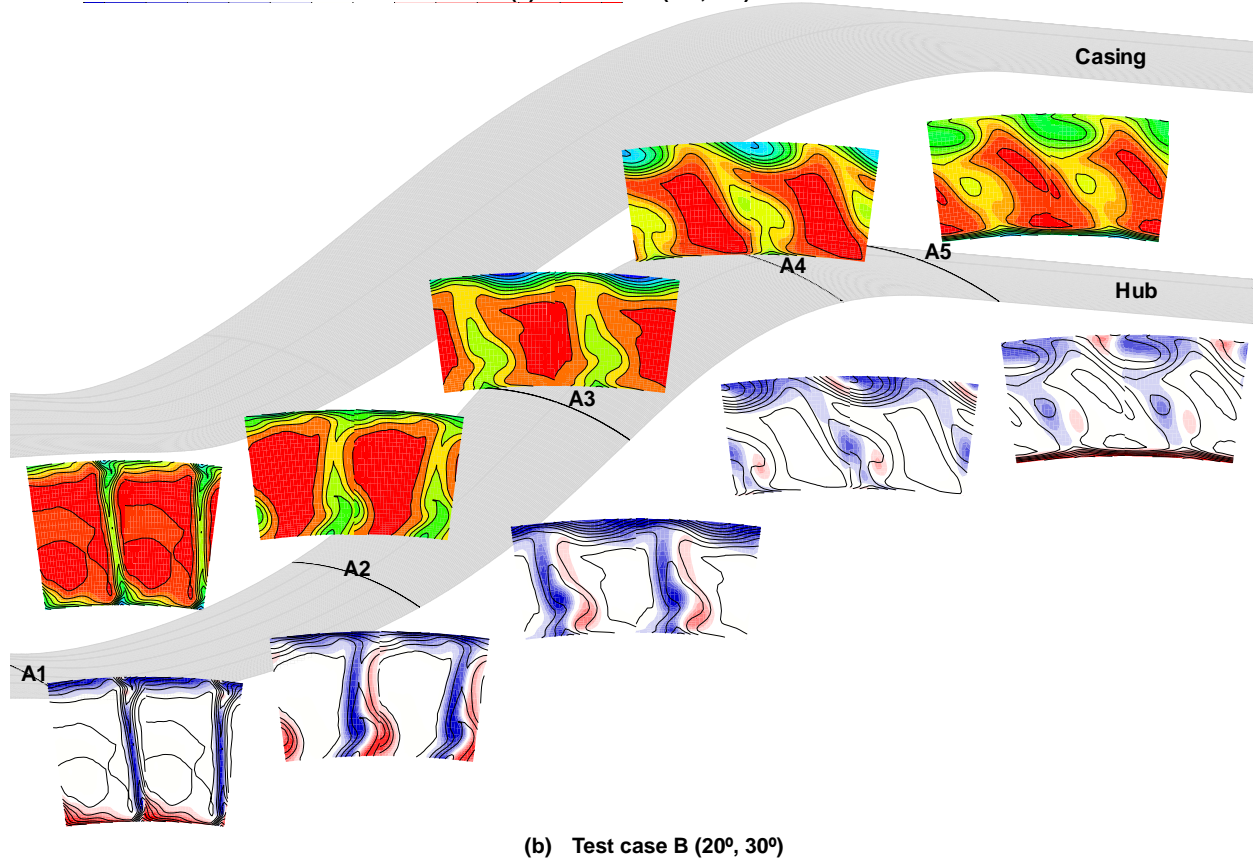
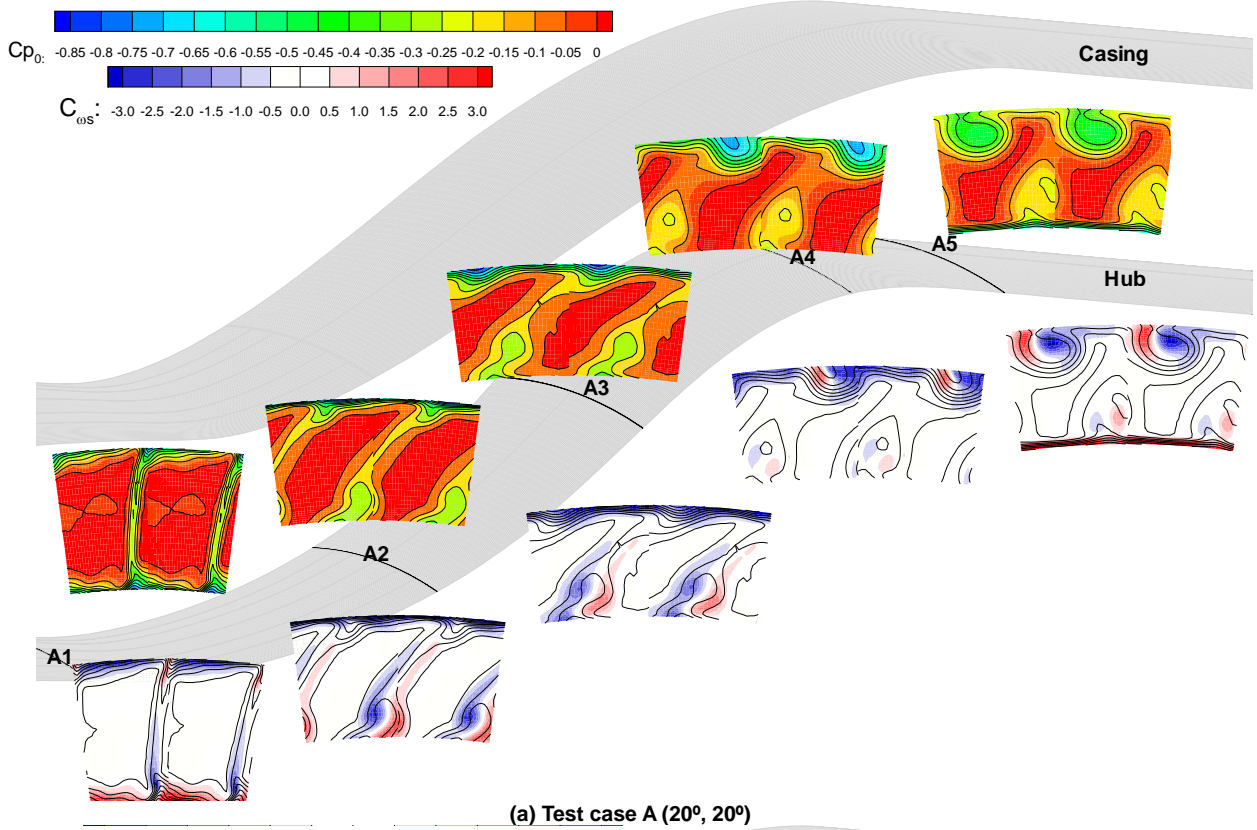
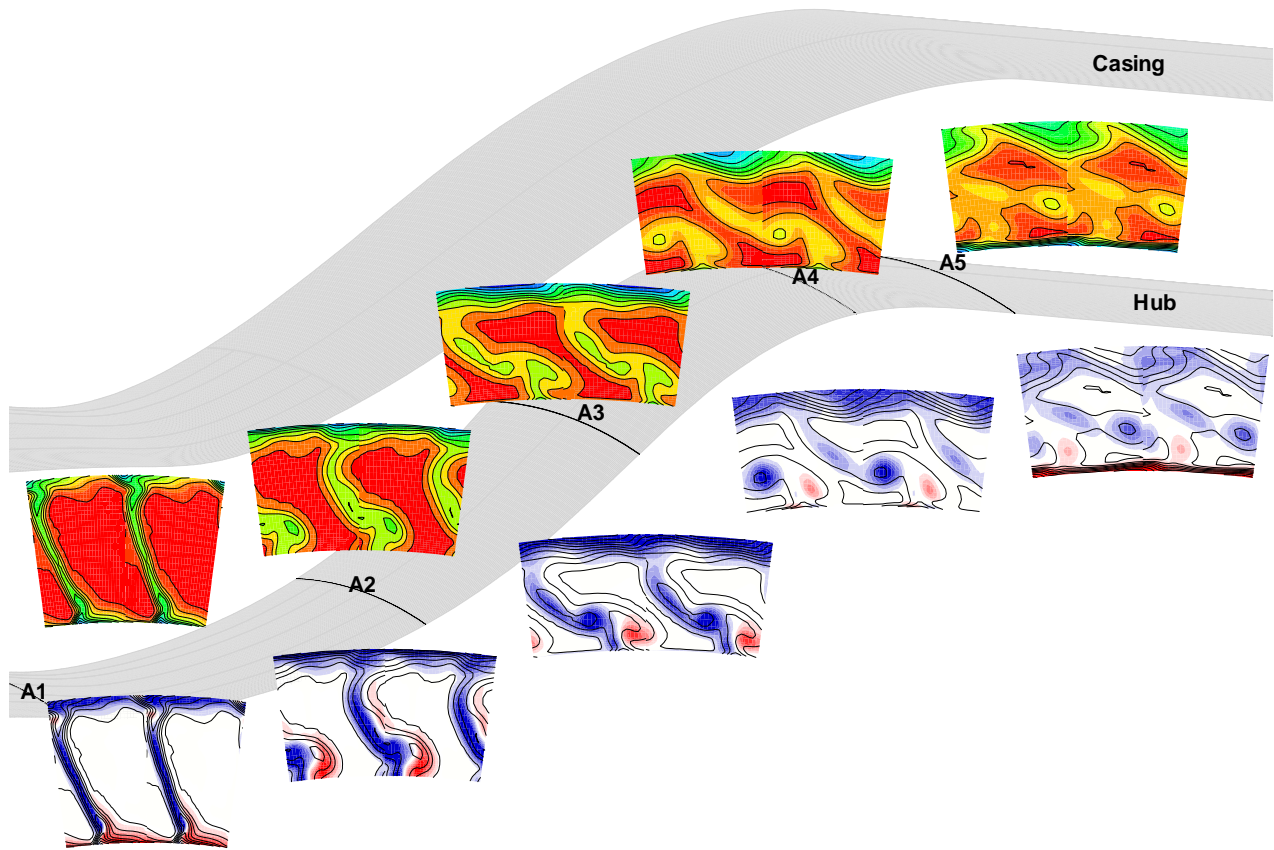


Figure 9. Measured total pressure coefficient C_{p_0} and streamwise vorticity coefficient C_{ws}



(c) Test case C (20°, 40°)

Figure 9. Measured total pressure coefficient C_{p0} and streamwise vorticity coefficient C_{ws} (continued)

When flow arrives at Location A3, the radial pressure gradient is smallest, and it is still hard to generate a pair of casing counter-rotating vortices. Hence only strong negative vorticity can be found in the casing region in all three cases. However, the casing 3D boundary layer is pronounced in test cases A and B, while in test case C the casing boundary layer contains very weak 3D feature. The wake skew angle in case A is still in clockwise direction with 25°. In case B and C, the wake skew angle is in counter-clockwise direction with 2° and 35°, respectively. The wake skew angle has a significant influence on the casing 3D boundary layer development. With smaller wake skew angle, the low momentum wake flow is easily moved into the casing boundary layer and causes a pronounced 3D casing boundary layer in test case B. Compared with that of case B, in case A, although the wake skew angle is larger, the first bend radial pressure gradient is also larger which results in a pronounced casing 3D boundary layer as well, as shown in Figure 9(a). In test case C, the wake skew angle is largest and the first bend radial pressure gradient is lowest, therefore, less low momentum flow is fed into the casing boundary layer. The casing boundary layer shows less 3D feature. Additionally, as shown in Figure 9(c), in case C the wake near the casing is almost mixed out at this

location. This also explains why in the flow visualization it is difficult to distinguish the wake at this location. On the other hand, the hub counter-rotating streamwise vortices are moving up in all cases and the strongest occurs in case C. The hub boundary layer continues to be thin in the three cases with the influence of the hub counter-rotating vortices and the hub favorable pressure gradient.

At Location A4, due to the reversed radial pressure gradient and the pronounced upstream casing 3D boundary layer, a pair of strong casing counter-rotating streamwise vortices is generated in both test cases A and B. Comparing them, the stronger vortex is found in case A. The first reason for this is because of the higher second bend radial pressure gradient in case A. The second reason is that the casing 3D separation occurs more upstream and is stronger in case A. This casing 3D separation enhances the 3D casing boundary layer development as well as the casing counter-rotating vortices. In test case C, due to the delayed casing 3D separation and the lowest second bend radial pressure gradient, the casing counter-rotating vortices are not that pronounced. At this Location, the wake skew angle in case A is 22° in clockwise direction. In cases B and C, the wake skew angle is further increasing in counter-clockwise direction with 5° and 40°, respectively. However, since the radial pressure gradient is reversed and no more low

momentum flow is fed into the casing boundary layer, the wake skew angle contributed little to the development of the casing 3D boundary layer. The hub counter-rotating vortices at this location still exist, but they are getting much weaker. Additionally, the hub boundary layer remains thin in all test cases.

At Location A5, the wakes are almost mixed out in all three cases. The flow within the ITD in the casing region is dominated by the casing counter-rotating vortices. In test case A and B, the casing counter-rotating vortices continue to grow. In test case C, the casing counter-rotating vortices are very weak, and the positive vorticity region is hard to detect. The hub counter-rotating streamwise vortices still exist at this location. It is noted that at this location the hub boundary layers are becoming thicker in all cases, and contain 3D features as well. The thick hub boundary layers are induced by the hub 3D boundary layer separation due to the local adverse pressure gradient as shown in Figure 5.

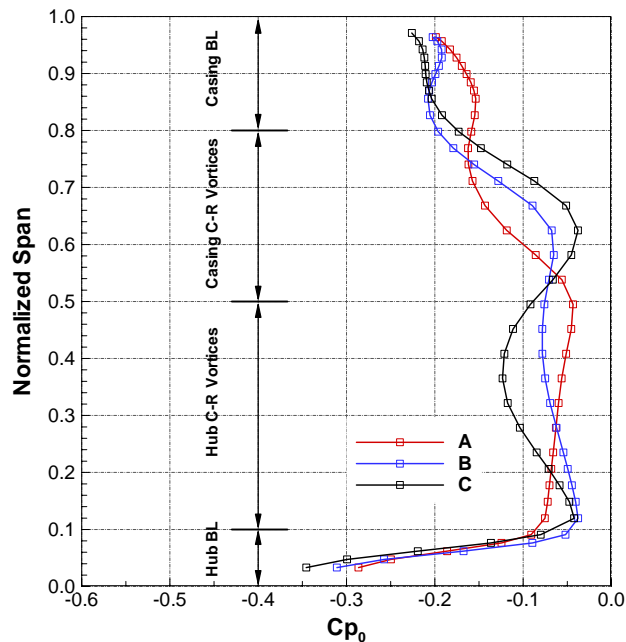


Figure 10. Pitchwise mass-averaged total pressure coefficients at Location A5

In order to examine the radial loss distribution, Figure 10 presents the pitchwise mass-averaged total pressure coefficients, Cp_0 , at different radial locations at Location A5 within the ITD for the three cases. Based on the flow physics within the ITD, the Cp_0 radial profiles are divided into four regions: hub boundary layer dominated region (0 to 20%), hub counter-rotating vortices dominated region (20% to 50%), casing counter-rotating vortices dominated region (50% to 80%), and casing boundary layer dominated region (80% to 100%). The losses in the casing counter-rotating vortices dominated region increase with decreasing casing swirl angle. However, the loss in the casing boundary layer dominated region decreases with decreasing casing swirl angle. On the other hand, in the hub region,

increasing the casing swirl, makes the hub counter-rotating vortices stronger and generates more loss in hub counter-rotating vortices dominated region. However, the loss in hub boundary layer dominated region is similar for all the three cases. It can be concluded that the loss within the ITD is significantly redistributed by the hub and casing vortices. The detail loss mechanism and comparison will be presented in Part II of this study.

CONCLUSIONS

This paper presents the detailed experimental and numerical results of an investigation on the inlet swirl influences on the flow development within an S-shaped ITD. The hub swirl is kept constant and the casing swirls are varied from 20° to 40° . Based on the numerical and experimental results, the flow development within the ITD is dominated by hub and casing counter-rotating vortices as well as the hub and casing 3D boundary layer separations.

In the casing region, the upstream vane casing vorticity field has slight influence on the ITD casing region flow field. However, because of the effects of the accumulating low momentum flow and the casing streamwise adverse pressure gradient, the casing boundary layer develops with highly 3D features. At the second bend, the casing counter-rotating vortices are generated and persist until the exit of the ITD. Furthermore, the casing 3D separation occurs first at the casing 3D boundary layer low momentum core region. The casing 3D separation enhances the 3D casing boundary layer development as well as the casing counter-rotating vortices. Additionally, the casing 3D separation is also influenced by the casing counter-rotating vortices. The boundary layer separation in the positive vorticity region is stronger.

With the variations of casing swirl angles, the static pressure distributions are changed correspondingly in both the hub and casing regions. The casing 3D boundary layer separation is delayed and weakened by increasing the casing swirl angle. The casing counter-rotating vortices are the strongest in the lowest casing swirl case (test case A) due to the strongest casing 3D boundary layer separation and the highest radial pressure gradient. Additionally, the casing 3D boundary layer development is significantly influenced by the wake skew angle. With higher wake skew angle, less low momentum flow will feed into the casing boundary layer and delay the 3D casing boundary layer development. On the other hand, although the hub swirl is kept constant, the hub counter-rotating vortices get stronger with the increasing inlet swirl gradient due to the stronger upstream wake vorticity. The total pressure coefficients within the ITD are significantly redistributed by hub and casing counter-rotating vortices.

ACKNOWLEDGMENTS

The authors wish to acknowledge the financial support of the National Research Council of Canada and Pratt & Whitney Canada. The technical support from Dr. Michael Benner, Dr. Ali Mahallati and Mr. Paul Hunt is greatly appreciated.

NOMENCLATURE

C_{p_0}	total pressure coefficient, $= (P_0 - P_{0ref}) / 0.5\rho V_{ref}^2$
C_{p_s}	static pressure coefficient, $= (P_s - P_{sA1}) / 0.5\rho V_{A1}^2$
x	axial coordinate
r	radial coordinate
t	tangential coordinate
V_x	axial velocity
V_t	tangential velocity
V_r	radial velocity
α^o	radial angle, $= \tan^{-1}(V_r/V_x)$
β^o	swirl angle, $= \tan^{-1}(V_t/V_x)$
ω_t	tangential vorticity
ω_x	axial vorticity
ω_s	streamwise vorticity
$C_{\omega s}$	streamwise vorticity coefficient

REFERENCES

- [1] Hu, S. Z., Zhang, X. F., Benner, M., Gostelow, P. and Vlastic, E., 2010, "Geometric Optimization of Aggressive Inter-turbine duct", ASME 14th International Mechanical Engineering Congress & Exposition, IMECE 2010-37323.
- [2] Bradshaw, P., 1976, "Effects of Steamline Curvature on Turbulent Flow", AGARD-AG-169.
- [3] Lohmann, R. P., Markowski, S. J., and Brookman, E. T., 1979, "Swirling Flow Through Annular Diffusers with Conical Walls", ASME J. Turbomach, Vol 101, pp. 224-228
- [4] Kumart, D. S., and Kumart, K. L., 1980, "Effect of Swirl on Pressure Recovery in Annular Diffusers", Journal Mechanical Engineering Science, Vol 22, No.6, pp. 305-313
- [5] Miller, R. J., Moss, R. W., Ainsworth, R. W., and Harvey, N. W., 2003, "The Development of Turbine Exit flow in a Swan-Necked Inter-Stage Diffuser", ASME Paper GT2003-38174.
- [6] Miller, R. J., Moss, R. W., Ainsworth, R. W., and Harvey, N. W., 2004, "The Effect of an Upstream Turbine on a Low-Aspect Ratio Vane", ASME Paper GT2004-54017.
- [7] Marn A., Göttlich E., Pecnik R., Malzacher F. J., Schennach O. and Pirker H. P., 2007, "The Influence of Blade Tip Gap Variation on The Flow Through an Aggressive S-Shaped Intermediate Turbine Duct Downstream of a Transonic Turbine Stage – Part I: Time-Averaged Results", ASME Paper GT2007-27405.
- [8] Göttlich E., Marn A., Pecnik R., Malzacher F. J., Schennach O. and Pirker H. P., 2007, "The influence of blade tip gap variation on the flow through an aggressive S-shaped intermediate turbine duct downstream of a transonic turbine stage – Part II: Time-averaged results and surface flow", ASME Paper GT2007-28069.
- [9] Marn, A., Göttlich, E., Malzacher F. and Pirker, H.P., 2009, "The Effect of Rotor Tip Clearance Size onto the Separation Flow Through a Super-Aggressive S-shaped Intermediate Turbine Duct Downstream of a Transonic Turbine Stage", ASME Paper GT2009-59934.
- [10] Dominy, R. G., and Kirkham, D. A., 1995, "The Influence of Swirl on the Performance of Inter-Turbine Diffusers", VDI Berichte 1186, pp. 107-122.
- [11] Dominy, R. G., and Kirkham, D. A., 1996, "The Influence of Blade Wakes on the Performance of Inter-Turbine Diffusers", ASME J. Turbomach, Vol 118, pp. 347-352.
- [12] Dominy, R. G., Kirkham, D. A., and Smith A. D., 1998, "Flow Development Through Inter-turbine Diffusers", ASME J. Turbomach., Vol 120, pp. 298-304.
- [13] Bailey, D. W., and Carrotte, J. F., 1996, "The Influence of Inlet Swirl on the Flow within an Annular S-Shaped Duct", ASME Paper 96-GT-60.
- [14] Axelsson L.-U., Arroyo Osso C., Cadrecha D. and Johansson T. G., 2007, "Design, Performance Evaluation and Endwall Flow Structure Investigation of an S-shaped Intermediate Turbine Duct", ASME Paper GT2007-27650.
- [15] Axelsson, L.-U. and Johansson, T.G., 2008, "Experimental Investigation of the Time-Averaged Flow in an Intermediate Turbine Duct", ASME Paper GT2008-50829.
- [16] Zhang, X. F., Hu, S. Z., Benner, M., Gostelow, P. and Vlastic, E., 2010, "Experimental and Numerical Study on an Inter-turbine Duct", ASME 14th International Mechanical Engineering Congress & Exposition, IMECE 2010-37322.
- [17] Yaras, M. and Sjolander, S.A., 1990, "Development of the Tip-Leakage Flow Downstream of a Planar Cascade of Turbine Blades: Vorticity Field", ASME Paper 1990, Vol 112, 610-617.
- [18] Brookfield, J.M, Waitz, I.A. and Sell, J, 1996, "Wake Decay: Effect of Freestream Swirl", ASME Paper 96-GT-495.
- [19] Zhang, Y. F., Hu, S. Z., Zhang, X. F., and Vlastic, E., 2011, "Influence of Inlet Swirl Distributions on an Inter-Turbine Duct- Part II: Hub Swirl Variation", ASME Paper, IGTI GT2011-45555.